# Evaluation of the Weather Research and Forecasting model in the Durance Valley complex terrain during the KASCADE field campaign

Peter Christiaan Kalverla*

*Wageningen University, Meteorology and Air Quality Section, Wageningen, The Netherlands*

*Laboratoire de Modélisation des Transferts dans l'Environnement, CEA Cadarache, France*

Gert-Jan Duine

*Laboratoire de Modélisation des Transferts dans l'Environnement, CEA Cadarache, France*

*Laboratoire d'Aérologie, University of Toulouse, Toulouse, CNRS, France*

Gert-Jan Steeneveld

*Wageningen University, Meteorology and Air Quality Section, Wageningen, The Netherlands*

Thierry Hedde

*Laboratoire de Modélisation des Transferts dans l'Environnement, CEA Cadarache, France.*

**Corresponding author address:* P.C. Kalverla, Wageningen University, Meteorology and Air Quality Section, P.O. Box 47, 6700 AA Wageningen, the Netherlands.

E-mail: peter.kalverla@wur.nl

## ABSTRACT

In the winter of 2012-2013, the KASCADE observational campaign was carried out in southeast France in order to characterize the wind and thermodynamic structure of the (stable) planetary boundary layer (PBL). Data were collected with two micro-meteorological towers, a SODAR, a tethered balloon and radiosoundings. Here, we use this dataset to evaluate the representation of the boundary layer in the WRF model. Generally, we find that diurnal temperature range (DTR) is largely underestimated, there is a strong negative bias in both longwave radiation components, and evapotranspiration is overestimated. An illustrative case is subjected to a thorough model-physics evaluation. First, five PBL parameterization schemes and two land surface schemes are employed. We find a marginal sensitivity to PBL parameterization, while the sophisticated Noah land-surface model represents the extremes in skin temperature better than a more simple thermal diffusion scheme. In a second stage, we performed sensitivity tests regarding land-surface-atmosphere coupling (through parameterization of $z_{0h}/z_{0m}$), initial soil moisture content and radiation parameterization. Relatively strong surface coupling and low soil moisture content results in a larger sensible heat flux, deeper PBL and a larger DTR. However, the larger sensible heat flux is not supported by the observations. It turns out that for the selected case, a combination of subsidence and warm air advection is not accurately simulated, but this cannot fully explain the discrepancies found in the WRF simulations. The results of the sensitivity analysis reiterate the important role of initial soil moisture values.

## 1. Introduction

For impact studies concerning the incidental release of pollutants in industry, it is critical to understand and be able to predict the meteorological conditions that govern the dispersion of these pollutants. In this context, stable boundary layers (SBLs) in complex terrain constitute a challenging case, because under these conditions there is not a single dominant term in the equations of motion that ultimately establishes the flow. Instead, the actual flow field is the result of interactions of many processes on different scales (Mahrt 2014; Steeneveld 2014). Another challenge for model simulations in complex terrain is the limited representation of orographic features. At the same time, stable conditions form the most limiting conditions for dispersion, because vertical mixing is suppressed.

All the challenges mentioned above come together in the case of Cadarache, one of the research facilities of the French Commissariat à l'Energie Atomique et aux Energies Alternatives (CEA). Cadarache is situated in southeast France, in an area of moderately complex terrain where SBLs develop frequently. To acquire the data necessary for increased understanding of the flow and for model evaluation, the KASCADE (KAtabatic winds and Stability over Cadarache for the dispersion of Effluents) experiment was carried out here in the winter of 2012-2013. The campaign resulted in 23 successful intensive observational periods (IOPs) and a unique dataset including flux measurements and vertical profiles acquired with radiosoundings, SODAR and a tethered balloon. Duine (2015) thoroughly analysed the dataset and provided much insight into the SBL development and interacting valley flows.

In the current paper, we present and discuss our simulation results from the Weather Research and Forecasting (WRF) model (Skamarock and Klemp 2008) for the KASCADE observational period. Persistent model deficiencies were identified, and sensitivity analysis points out the importance of soil moisture and surface-coupling strength. Before we continue with our research objectives, we briefly review the literature on physical processes and previous modelling studies.

Stable boundary layers often develop during nights with clear skies and weak winds (Stull 1988). The net negative radiation budget leads to surface cooling and consequently, a cold layer of air gradually develops vertically. In this layer, vertical motion is suppressed by buoyancy effects and dispersion of pollutants is limited. The stable stratification is enhanced in complex terrain, where the denser air accumulates in the valleys, leading to the formation of cold pools (Price et al. 2011) and a strong temperature inversion at the interface between these cold pools and the warmer air aloft. Over both flat and complex terrain, if the density stratification becomes strong enough, turbulence can be completely suppressed by the buoyancy force and consequently, the large-scale flow can decouple from the local flow near the surface (Mahrt 1999). Related phenomena are low-level jets (e.g. Van de Wiel et al. 2010) and intermittent turbulence (Kondo et al. 1978; Medeiros and Fitzjarrald 2014). Another aspect relevant to this study that influence the flow in complex terrain are the development of diurnal mountain winds, where winds blow up-valley during the day and down-valley during the night (Zardi and Whiteman 2013). Forced and pressure-driven channeling, where the surface wind is directed parallel to the valley axis regardless of the wind direction aloft (Whiteman and Doran 1993; Carrera et al. 2009) may play a role as well.

Numerical weather prediction model performance for the SBL has been studied within the context of the GABLS model intercomparison studies (Holtslag et al. 2013). Roughly speaking, it was concluded that state-of-the-art models perform reasonably well for SBLs characterized by moderate stratification, but additional challenges arise when considering SBLs with very strong stratification and SBLs over heterogeneous terrain. Holtslag et al. (2013) also stressed that correct atmosphere-land-surface coupling is essential for a good representation of the diurnal cycle of the boundary layer. Previous WRF studies for complex terrain (e.g. Passner and Range 2007; Jiménez and Dudhia 2013; Gsella et al. 2014) found that near-surface winds are often overestimated and that model performance is sensitive to the synoptic situation. Under weak synoptic forcing, biases in wind speed and direction are largest. These studies ran WRF with a 2 or 3 km horizontal grid spacing and simulations were validated with standard meteorological observations. Jiménez and Dudhia (2013) note that the flow near the surface is the result of interactions between local effects and the large-scale flow and therefore the representation of orography is important for good model performance. Challenges in the representation of slopes are related to accurate representation of horizontal pressure gradients and diffusion (Zängl 2002; Weller and Shahrokhi 2014).

Motivated by the challenges mentioned above, the goal of the current study is to assess and optimize the capability of the WRF model to predict the meteorological conditions that control the dispersion of pollutants — wind, stability and mixing — at Cadarache and its surroundings. Initially, we focus on the role of the planetary boundary-layer (PBL) and land-surface parameterizations in the WRF model. We seek to answer the following questions: (1) which combination of PBL and land-surface parameterization is the most suitable for characterization of the PBL at Cadarache and (2) what are the strengths and weaknesses of the representation of key physical processes in the model simulations? Even though KASCADE focused specifically on SBLs, we find that the representation of the full diurnal cycle of the PBL shows persistent flaws. Most notably, the diurnal temperature range is underestimated. We select a typical case and perform sensitivity analyses to various model aspects. Here, we highlight three of them by answering the following questions: (1) what is the model sensitivity to land-surface coupling, in particular through the Zilitinkevich parameter (Zilitinkevich 1995) for the thermal roughness length $z_{0h}$, (2) can the model performance be improved by using different radiation parameterizations and (3) what is the influence of soil moisture in the initial conditions on model simulations?

Section 2 discusses the study area and explain the IOP selection. Section 3 summarizes the model set-up and Section 4 presents the model evaluation and sensitivity studies. Recommendations and conclusions are given in Section 5.

## 2. Study area and IOP selection

### *a. Study area*

Cadarache (43.69N, 5.76E) is located in southeast France (Figure 1), an area known for its clear skies, dry conditions, and large diurnal temperature range (DTR, e.g. Drobinski et al. 2005). The elevation of Cadarache is between 250-300 m above sea level and the Mediterranean Sea is located 60 km to the south. The orography in the area is dominated by moderately high mountain ridges of 1000-1250 m (Sainte Victoire, Luberon) and the middle Durance valley, which has a north-northeasterly directed 50 km long fetch. The valley depth varies, but is ~200 m close to the Cadarache site. Its width is 5-8 km (ridge to ridge) and the valley bottom has an average slope angle of 0.2°. 10 km downstream of Cadarache, the valley narrows to 200 m near Clue De Mirabeau. The Plateau de Valensole, a slight northeast-southwest oriented sloping plateau, separates the Durance valley from the Southern Alps. Cadarache is situated in a small side valley (the Cadarache Valley) of the Durance valley near the Clue de Mirabeau. This valley has a length of 6 km, a depth of ~100 m, a width of 1–2 km, and the valley-bottom slope angle is 1.2° (Figures 1C and D).

Soils in the area are rich in limestone and typical vegetation types are herbaceous shrubs, pine trees and evergreen oaks (Ganteaume et al. 2009). Due to the Mistral, a dry northerly wind that develops frequently, the skies are often very clear and sunshine is abundant throughout the year ( $>$ 2500 h, Wrathall 1985). The Mistral deflects to a northwesterly direction near Cadarache and may reach 30 m $s^{-1}$. Also, a northeasterly Durance down-valley wind is frequently observed at night (Duine et al. 2014). In a mature state, the Durance down-valley wind reaches 4-8 m $s^{-1}$. The mechanism of this wind is thought to be part of a mountain-plain wind system, such as explained in Zardi and Whiteman (2013, Ch. 2.5). In this hypothesis, the Durance valley drains the outflow of relatively cold air from the Alps. Local slope flows and/or channeling of the wind are considered to be governing mechanisms for the Durance down-valley wind.

### *b. The KASCADE dataset*

The observations from the KASCADE campaign (Duine et al. 2014) consist of continuous measurements on three sites (Figure 1C) with additional measurements obtained during 23 IOPs. Temperature (PT100) and wind (Metek sonic anemometer) are routinely observed at the top of a 110-m mast (GBA). This mast exceeds the depth of the Cadarache valley and thus measures the flow in the larger Durance valley. Furthermore, an automated weather station is situated at the northernmost edge of Cadarache (VER) which measures 2 m temperature, humidity and pressure and 15m wind speed. For the KASCADE campaign, this site was equipped with a Remtech PA2 SODAR, measuring wind speed and direction up to ~500 m. At the bottom of the Cadarache Valley a 30 m flux divergence tower was temporarily installed and equipped with sonic anemometers at three levels (Campbell Sci. CSAT at 30 m, Young 81000 at 10 and 2 m), one fast hygrometer (LI-COR LI-7500A) at 30 m, net radiometers at two levels (CNR4 at 20 m and CNR1 at 1.2 m, both Kipp&Zonen), and thermohygrometers at two levels (Campbell Sci. HMP45 at 30 m and Campbell Sci. HC2S3 at 1.90 m). Temperature, humidity and radiation components were sampled every 10 s and averaged over 10 min. The sonic anemometers and LI-COR sampled at 10 Hz. Turbulent fluxes like latent heat ($L_vE$), sensible heat ($H$) and momentum ($\tau$) were calculated using the EddyPro flux package® (LI-COR Biosciences, USA), version 4.1.2. During IOPs, radiosoundings

(MODEM M2K2-DC) were launched at 1200, 1800, 0000 (only the last 5 IOPs) and 0600 UTC and a tethered balloon (Vaisala TTS111) gathered nearly continuous profiles of wind speed and direction, temperature, humidity and pressure up to 300 m.

After the KASCADE campaign, all sensors have been checked for inconsistencies and re-calibrated during a two-month inter-comparison campaign at Centre de Recherche Atmosphériques, Lannemezan, France. The CNR1 radiometer was calibrated against the CNR4. The longwave radiation components from CNR4 have been checked additionally to a CG4 radiometer (Kipp & Zonen), no correction was needed. The thermohygrometers from the flux tower have been mutually corrected for humidity; for temperature, no correction was needed. For pressure of the tethersondes, the average was taken as reference for correction, while for relative humidity, they were corrected against the M30 thermohygrometers. At every start of a tethered balloon session, the tethersondes were calibrated for wind direction. The validity of calculated fluxes was checked during the inter-comparison campaign with an other eddy-covariance package (Baghi et al. 2012). The SODAR profiles have been calibrated against the tethered balloon measurements and 110 m mast. Additional information on the correction procedures can be found in Duine (2015).

Unfortunately, observations of the soil heat flux, $G$, were unavailable and we could not check the closure of the surface energy balance. However, using a simple empirical formula from De Rooy and Holtslag (1999), we estimated $G$ from observations of 2 m temperature. Using these estimates, we found that the energy balance does not close. For example at noon, the available energy at the surface ($Q^* - G$) is 100 W m$^{-2}$ larger than the energy that is used for heating and evapotranspiration ($H + L_v E$). This issue has already been addressed by, e.g., Twine et al. (2000) and Ingwersen et al. (2011) and should be kept in mind during the interpretation of the results.

### c. IOP selection and characterization

We have performed WRF model simulations for all KASCADE IOPs. For this paper, we selected the period between 1200 UTC 18 February 2013 - 1200 UTC 20 February 2013 as an illustrative example of our model evaluation, and we subjected this case to a thorough evaluation and sensitivity analysis. The period covers exactly two IOPs (15 and 16) and is nearly cloud-free, which favors the development of SBLs in which the most challenging flows occur. Another advantage is that we exclude uncertainties involved with the selected cumulus parameterization, which is outside the scope of this evaluation. The local time is UTC+1.

Figure 2 shows that the synoptic pressure gradient over the study area is small during the selected period. On 18 February 1200 UTC, a high-pressure area extends from the United Kingdom to the Black Sea. Together with a low-pressure system over the Atlantic, this results in a weak southeasterly flow over Cadarache. After 24 h, the anticyclone has disintegrated and low pressure areas over Poland and Greece induce a northeasterly flow over France, as confirmed by radiosoundings (not shown).

Figures 3A and B show contrasting wind patterns in the two IOPs. IOP15 (1200 UTC 18 Feb – 1200 UTC 19 Feb) starts with a south-southeasterly wind of 4–6 m $s^{-1}$ in the lowest 500 m. Around 2100 UTC 18, the wind speed decreases and the wind direction turns to northeast, starting from the surface, i.e. the typical Durance down-valley wind develops. During IOP16 (1200 UTC 19 Feb - 1200 UTC 20 Feb) the wind is much stronger, up to 10 m $s^{-1}$, and from the west-northwest, i.e. a rather weak manifestation of the Mistral. After sunset, wind speeds drop and the wind turns to the north and slightly northeast, but much less pronounced than in IOP15.

The descending isentropes in Figure 3C reveal warming of the upper air due to advection and/or subsidence (0.24 K $h^{-1}$ above 1500 m). Strong vertical gradients of potential temperature ($\theta$)

and humidity ($q$) are observed on 19 February (Figure 3D, see also Figure 6). The figure also depicts the development of the SBL and illustrates the large DTR. At 0600 UTC (both nights), $\theta$ drops to 270 K at the surface, while it reaches a maximum of 286 K at 19 February around noon. The lowest 200 m of the PBL has been subject to drying by dew formation at night (see also Figure 6D), while $q$ increases due to evapotranspiration during the daytime. The radiosonde launch site was located inside the Cadarache valley and accumulation of cold air in the valley enhances the nocturnal cooling near the surface. Note that Figures 3C and D are based on interpolation between radiosoundings and even though they give a first order estimate of the PBL evolution, the interpolated profiles of $\theta$ and $q$ are merely a simplification. For example, in the growth of the PBL during the day, the isentropes show a decreasing stable stratification in the morning of 19 February, while physically, one would expect a development of the PBL in the form of a layer of neutral stratification extending vertically from the surface (compare Figure 5).

## 3. Model configuration

This section summarizes our WRF (version 3.5.1) model configuration, covering the general settings (Section 3a, Table 1) and utilized land-surface (Section 3b, Table 2) and PBL schemes (Section 3c).

### *a. General settings*

The model set-up consists of four nested domains centered around Cadarache (Figure 4). The outer grid covers part of Europe with most of the boundaries over the Atlantic Ocean and the Mediterranean Sea. The second domain covers the Alps (partly), the Pyrenees, and the Massif Central. The third covers southeast France, and finally the fourth domain represents the Durance valley with the surrounding mountains. The grid spacing in the inner domain is 1 km. Figure 1C demonstrates that the Durance valley is quite well-represented at this 1 km-grid. The Cadarache valley, however, is smoothed and barely recognizable (not shown). Since most of the measurements were taken inside this valley, comparison of measurements and model results will not be straightforward, because local processes such as the accumulation of cold, dense air in the valley and sheltering of the wind will not be resolved by the model.

We chose the Corine Land Cover (Büttner et al. 2004) because it is more recent (2006) than the commonly applied USGS landuse (1992) and it has a finer grid spacing (100 m versus 900 m). To make the Corine data compatible with WRF, a reclassification table is used as in Pineda et al. (2004). We use the ECMWF operational analysis input data on a horizontal grid of 0.25° and on 20 vertical pressure levels. This horizontal grid spacing is approximately the same as in the WRF outer domain. The WRF model is employed with 35 vertical eta levels (see Figure 6C). In a sensitivity experiment we have tested the WRF model with 46, 51 and 63 levels with ECMWF data on 20 pressure levels and 63 model levels (Note that from the 91 model levels in the ECMWF model, 63 are located below the WRF model top at 50 hPa). We found marginal differences between the simulations and thus decided to use with the pressure levels and 35 WRF levels, which is substantially cheaper in terms of computational costs. We have also performed test simulations with GFS input data, but the GFS model often provided snow cover when it was not observed, and this led to large biases in model output. All general settings are listed in Table 1.

*b. Land surface parameterization*

The land-surface scheme plays a key role for the partitioning of the available energy at the surface. We use two schemes of contrasting complexity. The MM5 5-layer thermal diffusion (TD) scheme (Dudhia 1996) is a very elementary scheme, which only computes the temperature in the different soil layers. It excludes canopy, and soil moisture is based on climatological data.

In contrast, the unified Noah land-surface model (Tewari et al. 2004) is more advanced, includes canopy, root penetration depth, soil moisture freezing, a layer of snow and surface runoff. Also, it calculates soil moisture prognostically. The representation of soil moisture in mesoscale models is essential (Chen and Dudhia 2001; Angevine et al. 2014) and we expect that this difference between the two surface schemes will have a large influence on the model results. Freezing of the top soil was often observed during KASCADE, which is another reason to expect better results from the runs with the Noah scheme.

### *c. PBL parameterization*

The PBL scheme computes the vertical transport of heat, water vapor and momentum due to turbulent mixing. In the Reynolds-averaged momentum equations, the contribution of vertical turbulent mixing to the time rate of change of an arbitrary variable $C$ can be expressed as (Stull 1988):

$$\frac{\partial C}{\partial t} = -\frac{\partial \overline{w'C'}}{\partial z} \; . \tag{1}$$

where $\overline{w'C'}$ is the (unknown) turbulent flux. In the following, we will describe different parameterizations to estimate this flux.

#### 1) Non-local closure

The first two schemes are YSU (Hong et al. 2006) and ACM2 (Pleim 2007). These are so-called first-order schemes, meaning that all first-order moments (turbulent averages) are explicitly resolved while all higher-order moments (variances and covariances) are parameterized. The turbulent term in equation (1) is directly related to the gradient of the variable $C$:

$$\overline{w'C'} = -K_C \frac{\partial C}{\partial z} \; , \tag{2}$$

where $K_C$ is the eddy diffusivity for $C$. As large eddies on the order of PBL height contribute substantially to energy transport, both schemes incorporate a non-local transport term under unstable conditions. For YSU, this is formulated as:

$$\frac{\partial C}{\partial t} = \frac{\partial}{\partial z}\left[K_C(\frac{\partial C}{\partial z} - \gamma_C) - \overline{(w'C')}_h(\frac{z}{h})^3\right] . \tag{3}$$

where $\gamma_C$ is a so-called ‘countergradient term’, which is proportional to the surface $H$ and inversely proportional to a velocity scale and the PBL height $h$. The last term represents entrainment at the PBL top. Alternatively, ACM2 represents non-local fluxes via ‘transilient turbulence theory’ (Stull 1993). This theory extends local closure as it suggests that the diffusivity approach can be used to compute the turbulent fluxes between a certain level $i$ and *any* other level, instead of only the two nearest neighbors. ACM2 uses a simple implementation of this theory, where only transport between adjacent layers is considered. Mathematically, this scheme takes the form:

$$\frac{\partial C_i}{\partial t} = f\left(M^{\uparrow}C_1 - M_i^{\downarrow}C_i + M_{i+1}^{\downarrow}C_{i+1}\frac{\Delta z_{i+1}}{\Delta z_i}\right) + \frac{\partial}{\partial z}\left(K_C(1-f)\frac{\partial C_i}{\partial z}\right) , \tag{4}$$

where first-order closure for local mixing can be recognized in the last term on the rhs. The other terms represent the non-local transport and the factor $f$ determines the relative contributions of the local and non-local closure approach, which depend on stability (Xie et al. 2012). $M^{\uparrow}$ represents the mixing rate for convective upward transport, $M^{\downarrow}$ represents compensating downward mixing rates, and $\Delta z$ indicates the layer depth. $K_C$ is a function of the velocity scale $\omega_s$, the definition of which differs between the two models (Kleczek et al. 2014, their table 1)

### 2) TKE-closure

Alternatively we may parameterize the turbulent transport via a 1.5-order TKE-closure. We employ three TKE-schemes, namely MYJ (Janjic 1994), MYNN2.5 (Nakanishi and Niino 2006) and QNSE (Sukoriansky et al. 2005). In these schemes, $K_C$ is expressed as (Stensrud 2007):

$$K_C = \lambda \mathrm{TKE}^{0.5} , \tag{5}$$

where $\lambda$ is a length scale for turbulent mixing and TKE is calculated prognostically. Again, the definitions of $\lambda$ and hence $K_C$ differ between the models (see Kleczek et al. 2014, their table 2). TKE closure has the advantage that no a priori balance is assumed between TKE production and dissipation and also it allows for TKE advection, which is physically more realistic in some cases.

### 3) Previous WRF PBL studies

Even though there are large differences between PBL studies, there are some general findings that recur in literature. Non-local mixing schemes usually generate more entrainment, resulting in thicker, drier and warmer PBLs (Bright and Mullen 2002; García-Díez et al. 2013; Holtslag et al. 2013). On the other hand, TKE-closure schemes often outperform first-order closure schemes in the simulation of the SBL (Steeneveld et al. 2008; Shin et al. 2012; Kleczek et al. 2014), because the decay of turbulence after sunset is more gradual and the local schemes are less sensitive to strong gradients near the ground. García-Díez et al. (2013) performed an extensive seasonal evaluation of three PBL schemes: YSU, ACM2 and MYJ. They found a cold bias in summer and a warm bias in winter. The DTR was underestimated throughout the year. PBL growth is usually underestimated in all schemes (except for YSU when the PBL depth is below 1000 m). We anticipate the same underestimation for all schemes in our results. Moreover, both Steeneveld et al. (2011) and García-Díez et al. (2013) report a substantial overestimation of the turbulent surface fluxes. Shin and Hong (2011) evaluated four of the five schemes used in this study and found that the representation of surface variables in WRF is still uncertain, especially under stable conditions. Based on these findings, we expect that the model will have difficulties representing the large DTR.

## 4. Results and discussion

### *a. Modelled evolution of wind, temperature and humidity*

First we evaluate the modelled evolution of wind, temperature and humidity (Figure 5), based on the optimized settings that we found in this study (see shown below), i.e. Noah+YSU, RRTMG radiation and MM5 revised surface-layer scheme. This figure is based on the full simulation (including spin-up time) and is intended to give a general impression of the model performance and to provide guidance during the discussion of the results. Therefore, only some salient features will be noted here. Note that comparison with Figure 3 is not straightforward, because (1) Figures 3C and D are based on interpolation of radiosoundings which have a much coarser temporal resolution and (2) due to the smoothing of orographic features, the 'surface' in the model may be displaced from the actual surface where the radiosoundings were launched and where the SODAR was installed. In the following sections we will use vertical profiles and time series of relevant variables to evaluate the model simulations in more detail and we will focus mainly on 19 February 1200 UTC and 20 February 0600 UTC, which was well after the start of the simulation. All results shown are taken from the appropriate grid points in domain D04.

The general wind pattern is well captured by the model (Figures 5A and B), but a closer look reveals some differences between the model results and the observations. Between 1200 and 1800 UTC (during spin-up), the modelled wind direction is biased to the east, and on 20 February the north-northeast component is delayed with respect to the observations. Modelled wind speeds are overestimated on 19 February and do not decrease until 0300 UTC, whereas the observed wind speed decreases already around sunset.

WRF reproduces the effects of advection and subsidence to some extent (Figure 5C). E.g. the 288 K isentrope lowers to ~1000 m during the simulation, corresponding to the observations.

However, the observed warming and drying aloft is much stronger than in the model simulations. The effects of this model deficiency on boundary-layer development will be explored in more detail in Section 4b.

### *b. Evaluation of reference schemes*

To understand the model behavior, we first analyze the wind and thermodynamic profiles (Figure 6). We present the profiles at 1200 UTC 19 February and 0600 UTC 20 February to evaluate both the well-mixed daytime boundary-layer and the early-morning SBL. Thereafter, we will present the temporal evolution of the modelled radiation and energy balance and relate them to characteristics of the profiles. Reference height for all profiles is the local terrain elevation, which is different for the model and the observations. Where appropriate, we will note the influence of this difference.

At 1200 UTC the PBL extends to a height of ~1400 m (Figure 6A), where a strong capping inversion is apparent in the observations. The model fails to reproduce this strong capping inversion, but the PBL height is clearly underestimated and the capping inversion is smoothed (the difference in local terrain elevation at the launch site of the balloon and at the location where the PBL top is encountered, is about 40 m. The balloon has not left the Cadarache valley at this point). The configuration with Noah+ACM2 performs better than the other configurations on this aspect. Moreover, we find that the modelled mixed layer is 2–3°C too cold and at least 1 g kg$^{-1}$ too moist (Figure 6C). While the fact that WRF is unable to reproduce the strong inversion might be related to the limited number of vertical levels, we did not see considerable improvement upon addition of extra layers. The biases in temperature and moisture suggest that $H$ ($L_vE$) is too small (large, see Section 4.c.3) and/or entrainment at the PBL top is underestimated. Both are intimately connected with the underestimated PBL height (Van Heerwaarden et al. 2009).

Before, we noted that heating and drying of the upper air due to a combination of advection and subsidence was underestimated by WRF. To understand the impact of this bias, we employed a simple bulk model for mixed-layer development. A smaller initial temperature and moisture jump at the PBL top (coherent with underestimated advection/subsidence) results in a deeper and colder mixed-layer. Thus, the WRF model bias in PBL height could not be attributed to underestimated advection and subsidence, but the cold bias could. However, the cold bias was found for numerous IOPs, also when advection and subsidence were absent in the observations. Possible sources of model deficiencies that remain are heat partitioning at the surface and entrainment at the PBL top.

With the TD-scheme, skin temperature $T_s$ is highly underestimated and the cold and moist biases in the PBL are larger than in the Noah scheme. The observed wind profile (Figure 6E) shows a strong shear layer at the PBL top, a jet with a wind speed of 6 m s$^{-1}$ just below and another jet with a wind speed of 8 m s$^{-1}$ at 500 m. The model fails to reproduce the jet at 500 m, but simulates one less distinct wind speed maximum ~1200 m.

At 0600 UTC, observations reveal several layers. Between the surface and 200 m, a strong temperature stratification is present (Figure 6B). Between 200 and 450 m, the stratification is nearly neutral and between 450 and 600 m we find another strong inversion. This pattern of neutral and stable stratification repeats itself once more. The model simulations show a similar layering for all configurations, but temperatures throughout the vertical profile are higher than observed and the height and depth of these layers are not correct. The modeled near-surface cooling is confined to a much too shallow layer (about 50 m), the most likely explanation for this discrepancy is the accumulation of cold air in the Cadarache valley that is unresolved in WRF. We note that there is a large gradient between $T_s$ and the temperature of the lowest model level. In Section 4c we will investigate the role of the surface-layer scheme in this apparent lack of surface-atmosphere coupling.

Observed humidity shows a maximum at 200 m (Figure 6D). We recall from Figure 3D that $q$ increased during daytime over the PBL extent due to evapotranspiration. The peak value of 4 g kg$^{-1}$ in the 0600 UTC sounding reflects the late-afternoon moisture content of the PBL (Figure 6D). We infer that dew formation is responsible for the drying in the lower 200 m, while advection explains the drying above 200 m. Different model configurations are consistent, only the simulation with Noah and QNSE is approximately 3°C colder and 0.5 g kg$^{-1}$ drier near the surface than the other configurations and seems to produce some dew formation. In the next section, we will link this to earlier decoupling of the lower atmosphere in this configuration.

The observed wind profile (Figure 6F) shows a small maximum near the surface, related to a drainage flow in the Cadarache Valley, and another jet of about 4 m s$^{-1}$ in the stratified layer around 500 m. Some of the model runs produce jets at different altitudes and all runs agree on what seems to be the same jet that was simulated at 1200 UTC around 1200 m.

Overall, the simulation of the instantaneous wind profile is not very accurate. Shin and Hong (2011) also found that WRF had difficulties simulating a near-surface wind maximum and nocturnal decoupling. Noting that the wind profile is closely related to the stratification, we presume that the model representation of thermodynamic profiles must be improved in order to reproduce the observed wind profile. Therefore, we will focus on the PBL growth, DTR and strength of the capping inversion in the remainder of this study.

The DTR at 110 m amounts to 12°C in the observations and only 7°C in the model simulations (Figure 7A). The DTR bias at 2 m is even larger (8°C), probably due to the effect of unresolved orography. There is little difference between the land-surface and PBL parameterizations. Underestimation of the DTR was found for many KASCADE IOPs and is a general problem in many atmospheric model (Lindvall and Svensson 2015).

The surface net radiative cooling amounts to 60 W m$^{-2}$ in the observations, which is quite high and favourable for SBL development (Figure 7B). During the day, we find a negative bias in the longwave incoming radiation at the surface, LW$^{\downarrow}$, of about 20 W m$^{-2}$. Similar biases have previously been reported in Van der Velde et al. (2010), Sterk et al. (2013), Kleczek et al. (2014), and Svensson and Lindvall (2015) and occured consistently in all model simulations for the KASCADE campaign. Also the upward flux LW$^{\uparrow}$ is underestimated as a result of the underestimated $T_s$, while SW↑ was well represented. We note that some clouds have been observed in the beginning of IOP15 , but the model has not had much spin-up time at this point and therefore we will not discuss this aspect.

On 19 February 1200 UTC we find a cold $T_s$ bias of 10°C (not shown). At night this bias decreases and at 20 February 0600 UTC, underestimation of $T_s$ is only 0–2°C with better performance of the TD land-surface scheme.

The 10 m wind speed is highly overestimated (Figure 7C). As a reference, we also plotted the observations at 110 m. This illustrates that the model *does* capture the general evolution of the wind speed, which leads us to the conclusion that 10 m winds are overestimated in the model due to a lack of frictional drag near the surface. After sunset at 19 February, the wind speed at 110 m in the observations drops quickly, while the modelled wind at 110 m (not shown) remains strong (~10 m s$^{-1}$) until about 0300 UTC (in accordance with Figure 5). We attribute this drop in wind speed to the decay of turbulence and downward momentum transport. The friction velocity $u_*$ follows the wind pattern (Figure 7D). In turn, $u_*$ is used to estimate the surface exchange coefficients and thus we find the same errors propagating to $H$ and $L_vE$ (Figures 7E and F), with excessive mixing at noon and continuing after sunset until about 0300 UTC. Concerning these heat fluxes, Noah predicts higher $H$ while TD forecasts much higher $L_vE$. $L_vE$ is overestimated in both schemes, which could explain why the profile in Figure 6C is too moist and also why this bias was larger with TD. Inspection of the Bowen ratio, $B(= H/L_vE)$ reveals that at midday, Noah ($B = 1.7$) corresponds better to the observations ($B = 2.8$) than TD ($B = 0.5$). These values are averages over all PBL schemes. Overestimation of $L_vE$ was found for all KASCADE model simulations. We will investigate the influence of the soil moisture content on flux partitioning and dew formation in Section 4c3.

### *c. Modifications to the physics formulations*

We found that the model produces a too wet and too shallow PBL, a too small DTR, a bias in longwave radiation and an overestimation of the wind and turbulent mixing. We found marginal differences between the model results from the various PBL parameterizations. With respect to the land-surface parameterization, simulations with the Noah scheme seem more realistic than with the TD scheme, mainly due to excessive evapotranspiration of the latter. Also Jin et al. (2010) found that simulation of most atmospheric variables improved with the complexity of the land-surface model. Hence we decide to continue our research only with Noah+YSU, which is a commonly used configuration in modelling studies (e.g. LeMone et al. 2010; Ruiz et al. 2010; Steeneveld et al. 2011; Carvalho et al. 2012; Warrach-Sagi et al. 2013). We will perform sensitivity tests regarding surface coupling and radiation schemes and we will investigate the influence of initial soil moisture.

#### 1) Sensitivity to land-atmosphere coupling within the surface-layer scheme

Previous studies (e.g. Chen et al. 1997, 2010; Tastula et al. 2015) have emphasized the role of surface-layer coupling in land-atmosphere models. The choice for $z_{0,h}$, representing the roughness length for heat, is of critical importance.

$H$ depends on the difference between the surface $T_s$ and the atmospheric temperature $T_a$ and on the aerodynamic resistance $r_H$:

$$H = \frac{\rho c_p (T_s - T_a)}{r_H} , \tag{6}$$

where $\rho$ represents the density and $c_p$ the specific heat capacity of air. $r_H$ is usually calculated with the logarithmic wind profile and a correction for non-neutral conditions, based on similarity theory:

$$r_H = \frac{1}{\kappa u_*} \left[ \ln(\frac{z_{eff}}{z_0}) - \Psi_h(\frac{z_{eff}}{L}) \right] , \tag{7}$$

where $z_{eff}$ is the chosen height (usually the first model level), $\kappa$ is the Von Karman constant (0.4) and $L$ is the Obukhov length. $z_0$ is the roughness length for momentum and is interpreted as the level at which the wind speed vanishes. However, there is an additional resistance for heat transport, that originates from the consideration that heat transfer between the surface and $z_0$ must be governed by molecular diffusion, which is a much less efficient process than turbulent transport. Note that in this so-called viscous sublayer, momentum transport can occur through pressure perturbations but heat transport cannot. Therefore, an additional resistance is added in Equation (7):

$$r_H = \frac{1}{\kappa u_*} \left[ \ln(\frac{z_{eff}}{z_0}) - \Psi_h(\frac{z_{eff}}{L}) + \ln(\frac{z_0}{z_{0h}}) \right] . \tag{8}$$

If $z_{0h} = z_0$, molecular diffusion is effective up to $z_0$ and there is no extra resistance. If $z_{0h} < z_0$, there is a large extra resistance because neither turbulence nor molecular diffusion is effective in the layer between $z_0$ and $z_{0h}$. Numerous proposed parameterizations relate $z_{0h}$ to flow characteristics (Chen et al. 1997) or canopy height (Chen and Zhang 2009, available option in WRF 3.5.1). A commonly used formulation is that of Zilitinkevich (1995):

$$\frac{z_0}{z_{0h}} = \exp(\kappa C_{zil} Re_*^{0.5}) , \tag{9}$$

where $Re_*$ is the roughness Reynolds number and $C_{zil}$ is an empirical coefficient. Trier et al. (2011) used typical values of the Zilitinkevich coefficient between 0.01 (large $z_{0h}$, strong coupling) and 1.0 (small $z_{0h}$, weak coupling). Yang et al. (2008), hereafter Y08, proposed an alternative formulation, which in their case resulted in better representation of $T_s$, $H$ and $L_vE$:

$$z_{0h} = \frac{70\nu}{u_*} \exp(-7.2 u_*^{0.5} |T_*|^{0.25}) \ , \tag{10}$$

where $\nu$ is the molecular viscosity of air and $T_*$ is a dimensionless temperature scale, i.e. $-\overline{w'T'}/u_*$.

We explore the sensitivity of WRF to the surface coupling strength by using $0.01 < C_{zil} < 1.0$. Also, we run a simulation with canopy dependent formulation (Chen et al. 1997) and we test the formulation of Y08. Finally, we run the model with a revised surface-layer (referred to as sfclay_rev in Table 3) formulation. The modifications in this last scheme, explained in Jiménez et al. (2012), make artificially enforced limitations unnecessary (e.g., in the previous formulation $u_*$ was limited to 0.1 m s$^{-1}$) and should improve the similarity functions.

We evaluate the variables that we find most suitable to illustrate the model's behavior (Table 3). Following Taylor (2001), we assess the root mean square difference split up in a centered part and a mean overall bias, and the correlation coefficient and normalized variance. Variance can be interpreted as a measure for the amplitude of the diurnal cycle in this case. The results with the canopy-dependent $C_{zil}$ (not shown) were similar to strong coupling ($C_{zil} = 0.01$).

We find that strong surface coupling (low $C_{zil}$) improves wind and temperature profiles, but at the cost of $T_s$ (through LW$^\uparrow$) and $H$ and LvE. For example, the peak of $H$ at noon is 190 W m$^{-2}$ in the strong coupling run versus 145 W m$^{-2}$ in the observations (not shown); in the weak coupling, it is only 75 W m$^{-2}$. In the strong coupling run, we find stronger dew formation at night. This is an encouraging result and we will see shortly that it also improves the simulation of the early morning moisture profile. Y08 better represents $H$ but some correlation, especially with the wind pattern is lost (Table 3). Hence, we do not consider this scheme as a general improvement to the model performance. Finally, we find that the revised scheme (sfclay_rev in Table 3) differs only slightly from the original scheme, but as its physical basis is more complete, we decide to retain this setting in all following simulations.

The difference in temperature at 1200 UTC between the extremes of $C_{zil}$ is approximately 1°C (Figure 8), while humidity varies by about 0.5 g kg$^{-1}$. The stronger coupling only marginally affects the model results at that time. At night, the profile is slightly colder with stronger coupling, but most striking is the improved resemblance of the humidity profile at 0600 UTC. We now recognize the $q$ maximum in the measurements, directly linked to higher dew formation at night (not shown). The peak value of almost 4.5 g kg$^{-1}$ again resembles the humidity of the mixed layer at 1800 UTC. As $L_vE$ is also amplified by the stronger coupling, this value is now too high.

Stronger surface coupling thus results in larger heat fluxes during the day. This improves the simulation of wind and temperature profiles, but deteriorates the representation of $H$, $L_vE$ and $T_s$. It enhances dew formation, but also increases the overall bias in $q$. Overall, surface coupling alone cannot explain all biases that we found in the model. Our results are consistent with Shin and Hong (2011), who found that the influence of the surface-layer parameterization in WRF is most pronounced in the representation of surface variables.

#### 2) Sensitivity to the selected radiation scheme

We found a strong bias in the modelled surface longwave radiation fluxes. Previous studies indicated that the radiation scheme can have a significant influence on the model results (Iacono and Nehrkorn 2010; Seefeldt et al. 2012; Karlický 2013). To assess the influence of the radiation scheme on our simulation, we test 3 alternative radiation configurations: Goddard shortwave

(Chou and Suarez 1994) and RRTM longwave, CAM (Collins et al. 2004) shortwave and longwave, and RRMTG (Iacono et al. 2008) shortwave and longwave (Figure 9).

It appears that in the configuration with CAM radiation, the clouds that were observed early in IOP15 are simulated, while the other configurations fail to reproduce these clouds. However, the $LW^{\downarrow}$ bias in the CAM simulation is larger than in the other schemes. The configuration with RRTMG slightly improves the overall bias in $LW^{\downarrow}$ (-16 versus -18 W m$^{-2}$ in the reference run). However, the maximum difference is still 20 W m$^{-2}$. Overall, longwave radiation components and $T_{110}$ improve slightly for the configurations with Goddard and with RRMTG, but this does not improve the representation of the other variables and the bias in most variables becomes larger. We conclude we cannot improve the overall model performance by changing the radiation parameterization. However, using RRTMG gives a slightly better representation of longwave radiation, so we decide to stick with this scheme for the final simulations.

### 3) Influence of soil moisture

Earlier we found that modeled evaporation is too high and the vertical humidity profile is too moist. A possible cause could be soil moisture values that are too high in the initial conditions that we used. Soils are generally dry in the study area, hence it would not be surprising if soil moisture is too high in the initial conditions. Indeed, the ECMWF operational analysis was found to generally overestimate soil moisture values, especially in dry areas (Albergel et al. 2012). 22 of the in situ measurement sites used in their study are in southern France (9 in the southeast). The important role of soil moisture in mesoscale modelling was recently emphasized in Angevine et al. (2014). Both $L_vE$ and soil heat conductivity depend on soil moisture. Lower soil moisture would result in a lower soil conductivity, lower $L_vE$ and thus higher $T_s$ and a larger $H$. In turn, a larger $H$ would result in more PBL growth and a warmer mixed layer (Van Heerwaarden et al. 2009). To assess the influence of the initial soil moisture fields on our simulation, we manually reduced the soil moisture field in the surroundings of Cadarache by multiplying with a factor 0.5.

Figures 10E and F show that the reduction of soil moisture has a large influence on the partitioning of the heat fluxes. $L_vE$ is now underestimated by more than 20 W m$^{-2}$, while $H$ is overestimated by 120 W m$^{-2}$. The larger $H$ results in a slightly higher PBL. The PBL is ~0.2 g kg$^{-1}$ drier at noon, but at night there is little difference. Dew formation is not enhanced, like it was in the run with stronger coupling. While the temperature profile and DTR improved by ~1 °C, the wind at 10 and 110 m is not much influenced by the soil moisture change, and $T_s$ at noon is even slightly overestimated (not shown).

### *d. Final remarks*

Our soil moisture experiment demonstrates that the model results are quite sensitive to the representation of soil moisture in the initial conditions, which is in agreement with earlier findings (e.g. Chow et al. 2006). This might also explain the differences we found between the Noah and TD schemes. To further investigate this aspect, observations of soil moisture should be used to verify and, if necessary, adjust the quality of the initial conditions. In a modelling study concerning the afternoon transition (related to BLLAST), Lothon et al. (2014) found that the spatial representation of soil moisture can be improved by performing a WRF 'spin-up' simulation of one month, and using the resulting soil moisture fields as initial conditions for the final WRF simulations. It would be interesting to perform a similar study for the Cadarache.

The combined effect of advection and subsidence resulted in a strong temperature inversion that was not accurately simulated by the model. The synoptic situation, however, was quite well represented in WRF and closer inspection of the vertical profiles revealed that the effects of advection and subsidence were present in the simulation as well, though less pronounced and delayed with respect to the observations. The inability of WRF to simulate the strong inversion may have to do with our choice of vertical levels. We have performed additional simulations with an increased vertical grid spacing with up to 51 levels, but this did not improve our results. Billings et al. (2006) used 100 levels in a similar sensitivity experiment and came to the same conclusion. Other mesoscale modelling studies used even finer vertical grids (e.g. Cuxart et al. 2007). This might be useful for studies aimed at understanding the flow characteristics, but the high computational cost makes it unsuitable for operational use.

In our experiments with respect to surface coupling and soil moisture, we have shown that increased surface heat fluxes can improve the boundary layer temperature and moisture profiles. To achieve a perfect correspondence between the model and the observations, however, the fluxes need to be much higher. Even if one takes a large measurement uncertainty and the effects of unresolved orography into account, this cannot be justified by the observations. Therefore, we suspect that underestimation of entrainment plays an important role as well.

While we focused on DTR, PBL height and flux partitioning at the surface, we have dedicated few words to the vertical representation of the wind in the Durance valley. Unfortunately, we have not found any improvement in the simulation of the low-level jets that were observed around 500 m in this study. We further studied the typical Durance down-valley wind and its representation in WRF, and it turns out that in general, the model simulations correspond quite well to the measurements. A detailed treatment of this subject, however, is outside the scope of this paper and further information can be found in Duine (2015). This document also describes the model results for other IOPs, where we found similar biases in DTR, longwave radiation and flux partitioning at the surface.

## 5. Summary and conclusions

SBL formation in complex terrain is both difficult to understand and to represent in atmospheric models. Channeled winds, cold-pool formation, elevated valley inversions, katabatic winds and flow decoupling are only a few of the phenomena that characterize the complex atmospheric behavior imposed by these conditions. At the same time, stratified conditions form the largest threat in case of incidental release of pollutants, because dispersion is limited by the stable stratification.

To evaluate the capability of the WRF model to represent these challenging conditions, we studied the evolution of the boundary layer in an area of complex terrain in southeast France: a dry area characterized by a large DTR where stable conditions occur frequently. For validation we used the KASCADE dataset, which was obtained in 2013 to facilitate impact studies.

In all simulations, the model highly underestimates the DTR and longwave radiation components. Generally, the latent heat flux is positively biased, resulting in too moist boundary layers. An illustrative case was subjected to an in-depth analysis. For this case, advection was underestimated by the model, and the convective boundary layer was too shallow. The bias in the incoming longwave radiation was as large as -18.5 W $m^{-2}$, consistent with earlier research. We found only a small sensitivity to the selected PBL parameterization and radiation. The Noah land surface scheme simulated $T_s$ better than the MM5 5-layer thermal diffusion (TD) scheme. With both schemes, evaporation is overestimated, but to a much larger extent in the TD scheme.

Focusing on a commonly used configuration in WRF, Noah+YSU, we explored the sensitivity to the strength of atmosphere-surface coupling by varying the Zilitikevich parameter $C_{zil}$ for $z_{0h}/z_{0m}$. Only with very strong coupling ($C_{zil} = 0.01$) did we find more realistic dew formation at night. Also, the shape of the temperature profile improved with stronger coupling at daytime, with a higher mixed layer and a stronger inversion, although this was only a minor improvement with respect to the original simulation. At the same time, sensible and latent heat fluxes were even more overestimated, at the cost of the diurnal range of $T_s$. Finally, a reduced soil moisture content resulted in a higher mixed layer, a stronger capping inversion and a slightly drier vertical moisture profile. Even though the PBL was still too shallow and 1 g kg$^{-1}$ too moist and the bias in the sensible heat flux increased substantially (135 W m$^{-2}$ larger than observed), these results confirm that initial soil moisture fields have an important influence on the model results and should be verified during the configuration of the WRF model.

Future studies will use the current model results to study the local flow patterns such as the Durance down-valley wind, taking into consideration the model deficiencies that we identified in this study. Such studies would largely contribute to the understanding of valley winds, cold pooling, and boundary-layer evolution over complex terrain in general and specifically to the understanding of the complex atmospheric behavior in the Durance valley. Researchers planning to perform a similar study can benefit from our findings.

*Acknowledgments.* We gratefully acknowledge Reinder Ronda and Leo Kroon for their valuable feedback and time spent. We thank the four reviewers for their constructive feedback on the manuscript. The KASCADE field experiment was made possible thanks to the contributions of several institutions and supports: CEA is thanked for the financial support, Laboratoire d'Arologie (LA, University of Toulouse) and LPCA (University of Dunkerque) are thanked for the provision of instrumentation. Finally, the European Centre for Medium-Range Weather Forecasts (ECMWF) is acknowledged for providing the operational analysis data that where used to initialize our simulations.

# References


Albergel, C., P. De Rosnay, G. Balsamo, L. Isaksen, and J. Munoz-Sabater, 2012: Soil moisture analyses at ECMWF: Evaluation using global ground-based in situ observations. *J. Hydrometeor.*, **13 (5)**, 1442–1460.

Angevine, W. M., E. Bazile, D. Legain, and D. Pino, 2014: Land surface spinup for episodic modeling. **14 (15)**, 8165–8172.

Baghi, R., and Coauthors, 2012: A new disjunct eddy-covariance system for BVOC flux measurements – validation on $CO_2$ and $H_2O$ fluxes. *Atmos. Meas. Techn.*, **5 (12)**, 3119–3132.

Billings, B. J., V. Grubišic, and R. D. Borys, 2006: Maintenance of a mountain valley cold pool: A numerical study. *Mon. Wea. Rev.*, **134 (8)**, 2266–2278.

Bright, D. R., and S. L. Mullen, 2002: The sensitivity of the numerical simulation of the southwest monsoon boundary layer to the choice of PBL turbulence parameterization in MM5. *Wea. Forecasting*, **17 (1)**, 99–114.

Büttner, G., J. Feranec, G. Jaffrain, L. Mari, G. Maucha, and T. Soukup, 2004: The CORINE land cover 2000 project. *EARSeL eProceedings*, **3 (3)**, 331–346.

Carrera, M. L., J. R. Gyakum, and C. A. Lin, 2009: Observational study of wind channeling within the St. Lawrence River Valley. *J. Appl. Meteor. Climatol.*, **48 (11)**, 2341–2361.

Carvalho, D., A. Rocha, M. Gómez-Gesteira, and C. Santos, 2012: A sensitivity study of the WRF model in wind simulation for an area of high wind energy. *Environmental Modelling & Software*, **33**, 23–34.

Chen, F., and J. Dudhia, 2001: Coupling an advanced land surface-hydrology model with the Penn State-NCAR MM5 modeling system. Part I: Model implementation and sensitivity. *Mon. Wea. Rev.*, **129 (4)**, 569–585.

Chen, F., Z. Janjić, and K. Mitchell, 1997: Impact of atmospheric surface-layer parameterizations in the new land-surface scheme of the NCEP mesoscale Eta model. *Bound.-layer Meteor.*, **85 (3)**, 391–421.

Chen, F., and Y. Zhang, 2009: On the coupling strength between the land surface and the atmosphere: From viewpoint of surface exchange coefficients. *Geophys. Res. Lett.*, **36 (10)**.

Chen, Y., K. Yang, D. Zhou, J. Qin, and X. Guo, 2010: Improving the Noah land surface model in arid regions with an appropriate parameterization of the thermal roughness length. *J. Hydrometeor.*, **11 (4)**, 995–1006.

Chou, M.-D., and M. J. Suarez, 1994: An efficient thermal infrared radiation parameterization for use in general circulation models. *NASA Tech. Memo*, **104606 (3)**, 85.

Chow, F. K., A. P. Weigel, R. L. Street, M. W. Rotach, and M. Xue, 2006: High-resolution large-eddy simulations of flow in a steep alpine valley. part i: Methodology, verification, and sensitivity experiments. *J. Appl. Meteor. Climatol.*, **45 (1)**, 63–86.

Collins, W. D., and Coauthors, 2004: Description of the NCAR community atmosphere model (CAM 3.0). Technical Note TN-464+ STR, National Center for Atmospheric Research, Boulder, CO, 214 pp.

Cuxart, J., M. Jiménez, and D. Martínez, 2007: Nocturnal meso-beta basin and katabatic flows on a midlatitude island. *Mon. Wea. Rev.*, **135 (3)**, 918–932.

De Rooy, W. C., and A. A. M. Holtslag, 1999: Estimation of surface radiation and energy flux densities from single-level weather data. *J. Appl. Meteor.*, **38 (5)**, 526–540.

Drobinski, P., and Coauthors, 2005: Summer mistral at the exit of the rhône valley. *Quart. J. Roy. Meteor. Soc.*, **131 (605)**, 353–375.

Dudhia, J., 1989: Numerical study of convection observed during the winter monsoon experiment using a mesoscale two-dimensional model. *J. Atmos. Sci.*, **46 (20)**, 3077–3107.

Dudhia, J., 1996: A multi-layer soil temperature model for MM5. Preprints of the Sixth PSU/NCAR Mesoscale Model Users's Workshop, 22-24 July 1996, Boulder, Colorado, 49-50.

Duine, G.-J., 2015: Characterization of down-valley winds in stable stratification from the KASCADE field campaign and WRF mesoscale simulations. Ph.D. thesis, Université Toulouse III Paul Sabatier.

Duine, G.-J., and Coauthors, 2014: Stable boundary layer characterization in an orographic complex region: the field measurement campaign KASCADE. *21st Symposium on Boundary Layers and Turbulence*, Leeds UK, June 09-13, 2014, 8B.2, URL https://ams.confex.com/ams/21BLT/webprogram/Paper245848.html.

Ganteaume, A., J. Marielle, L.-M. Corinne, C. Thomas, and B. Laurent, 2009: Fuel characterization and effects of wildfire recurrence on vegetation structure on limestone soils in southeastern France. *Forest ecology and management*, **258**, S15–S23.

García-Díez, M., J. Fernández, L. Fita, and C. Yagüe, 2013: Seasonal dependence of WRF model biases and sensitivity to PBL schemes over Europe. *Quart. J. Roy. Meteor. Soc.*, **139 (671)**, 501–514.

Gsella, A., A. de Meij, A. Kerschbaumer, E. Reimer, P. Thunis, and C. Cuvelier, 2014: Evaluation of MM5, WRF and TRAMPER meteorology over the complex terrain of the Po Valley, Italy. *Atmos. Env.*, **89**, 797–806.

Holtslag, A. A. M., and Coauthors, 2013: Stable atmospheric boundary layers and diurnal cycles: challenges for weather and climate models. *Bull. Amer. Meteor. Soc.*, **94 (11)**, 1691–1706.

Hong, S.-Y., and J.-O. J. Lim, 2006: The WRF single-moment 6-class microphysics scheme (WSM6). *J. Korean Meteor. Soc*, **42 (2)**, 129–151.

Hong, S.-Y., Y. Noh, and J. Dudhia, 2006: A new vertical diffusion package with an explicit treatment of entrainment processes. *Mon. Wea. Rev.*, **134 (9)**, 2318–2341.

Iacono, M., and T. Nehrkorn, 2010: Assessment of radiation options in the advanced research WRF weather forecast model. *Proceedings of 1st atmospheric system research science team meeting*, Bethesda, MD, Office of Science, US Department of Energy, 15–19.

Iacono, M. J., J. S. Delamere, E. J. Mlawer, M. W. Shephard, S. A. Clough, and W. D. Collins, 2008: Radiative forcing by long-lived greenhouse gases: Calculations with the AER radiative transfer models. *J. Geophys. Res.: Atmospheres (1984–2012)*, **113 (D13)**.

Ingwersen, J., and Coauthors, 2011: Comparison of noah simulations with eddy covariance and soil water measurements at a winter wheat stand. *Agric. For. Meteor.*, **151 (3)**, 345–355.

Janjic, Z. I., 1994: The step-mountain eta coordinate model: Further developments of the convection, viscous sublayer, and turbulence closure schemes. *Mon. Wea. Rev.*, **122 (5)**, 927–945.

Jiménez, P. A., and J. Dudhia, 2013: On the ability of the WRF model to reproduce the surface wind direction over complex terrain. *J. Appl. Meteor. Climatol.*, **52 (7)**, 1610–1617.

Jiménez, P. A., J. Dudhia, J. F. González-Rouco, J. Navarro, J. P. Montávez, and E. García-Bustamante, 2012: A revised scheme for the WRF surface layer formulation. *Mon. Wea. Rev.*, **140 (3)**, 898–918.

Jin, J., N. L. Miller, and N. Schlegel, 2010: Sensitivity study of four land surface schemes in the WRF model. *Adv. Meteor.*, **vol. 2010**, 11 pages, doi:10.1155/2010/167436, article ID 167436.

Kain, J. S., 2004: The Kain-Fritsch convective parameterization: an update. *J. Appl. Meteor.*, **43 (1)**, 170–181.

Karlickỳ, J., 2013: Regional climate simulations with WRF model. *WDS'13 Proceedings of Contributed Papers: Part III Physics*, 80–84, URL http://www.mff.cuni.cz/veda/konference/wds/proc/pdf13/WDS13_314_f8_Karlicky.pdf.

Kleczek, M. A., G.-J. Steeneveld, and A. A. M. Holtslag, 2014: Evaluation of the weather research and forecasting mesoscale model for GABLS3: Impact of boundary-layer schemes, boundary conditions and spin-up. *Bound.-layer Meteor.*, **152 (2)**, 213–243.

Kondo, J., O. Kanechika, and N. Yasuda, 1978: Heat and momentum transfers under strong stability in the atmospheric surface layer. *J. Atmos. Sci.*, **35 (6)**, 1012–1021.

LeMone, M. A., F. Chen, M. Tewari, J. Dudhia, B. Geerts, Q. Miao, R. L. Coulter, and R. L. Grossman, 2010: Simulating the IHOP_2002 fair-weather CBL with the WRF-ARW-Noah modeling system. Part I: Surface fluxes and CBL structure and evolution along the eastern track. *Mon. Wea. Rev.*, **138 (3)**, 722–744.

Lindvall, J., and G. Svensson, 2015: The diurnal temperature range in the cmip5 models. *Climate Dyn.*, **44 (1-2)**, 405–421.

Lothon, M., and Coauthors, 2014: The BLLAST field experiment: Boundary-layer late afternoon and sunset turbulence. *Atmosph. Chem. and Phys.*, **14 (20)**, 10 931–10 960.

Mahrt, L., 1999: Stratified atmospheric boundary layers. *Bound.-layer Meteor.*, **90 (3)**, 375–396.

Mahrt, L., 2014: Stably stratified atmospheric boundary layers. *Annu. Rev. Fluid Mech.*, **46 (1)**, 23–45.

Medeiros, L. E., and D. R. Fitzjarrald, 2014: Stable boundary layer in complex terrain. Part I: Linking fluxes and intermittency to an average stability index. *J. Appl. Meteor. Climatol.*, **53 (9)**, 2196–2215.

Mlawer, E. J., S. J. Taubman, P. D. Brown, M. J. Iacono, and S. A. Clough, 1997: Radiative transfer for inhomogeneous atmospheres: RRTM, a validated correlated-k model for the longwave. *J. Geophys. Res.: Atmospheres (1984–2012)*, **102 (D14)**, 16 663–16 682.

Nakanishi, M., and H. Niino, 2006: An improved Mellor–Yamada level-3 model: Its numerical stability and application to a regional prediction of advection fog. *Bound.-layer Meteor.*, **119 (2)**, 397–407.

Passner, J. E., and W. S. M. Range, 2007: Performance of the WRF-ARW in the complex terrain of salt lake city. *12th Conference on Mesoscale Processes*.

Pineda, N., O. Jorba, J. Jorge, and J. M. Baldasano, 2004: Using NOAA AVHRR and SPOT VGT data to estimate surface parameters: application to a mesoscale meteorological model. *International Journal of Remote Sensing*, **25 (1)**, 129–143.

Pleim, J. E., 2007: A combined local and nonlocal closure model for the atmospheric boundary layer. Part I: Model description and testing. *J. Appl. Meteor. Climatol.*, **46 (9)**, 1383–1395.

Price, J., and Coauthors, 2011: Colpex: field and numerical studies over a region of small hills. *Bull. Amer. Meteor. Soc.*, **92 (12)**, 1636–1650.

Ruiz, J. J., C. Saulo, and J. Nogués-Paegle, 2010: WRF model sensitivity to choice of parameterization over South America: validation against surface variables. *Mon. Wea. Rev.*, **138 (8)**, 3342–3355.

Seefeldt, M. W., M. Tice, J. J. Cassano, and M. D. Shupe, 2012: Evaluation of WRF radiation and microphysics parameterizations for use in the polar regions. *AGU Fall Meeting Abstracts*, Vol. 1, 0091.

Shin, H. H., and S.-Y. Hong, 2011: Intercomparison of planetary boundary-layer parametrizations in the WRF model for a single day from CASES-99. *Bound.-layer Meteor.*, **139 (2)**, 261–281.

Shin, H. H., S.-Y. Hong, and J. Dudhia, 2012: Impacts of the lowest model level height on the performance of planetary boundary layer parameterizations. *Mon. Wea. Rev.*, **140 (2)**, 664–682.

Skamarock, W. C., and J. B. Klemp, 2008: A time-split nonhydrostatic atmospheric model for weather research and forecasting applications. *J. Computational Physics*, **227 (7)**, 3465–3485.

Steeneveld, G.-J., 2014: Current challenges in understanding and forecasting stable boundary layers over land and ice. *Frontiers in Environmental Science*, **2**, 41.

Steeneveld, G.-J., L. F. Tolk, A. F. Moene, O. K. Hartogensis, W. Peters, and A. A. M. Holtslag, 2011: Confronting the WRF and RAMS mesoscale models with innovative observations in the netherlands: evaluating the boundary layer heat budget. *J. Geophys. Res.: Atmospheres (1984–2012)*, **116 (D23)**.

Steeneveld, G.-J., J. Vilà-Guerau de Arellano, A. A. M. Holtslag, T. Mauritsen, G. Svensson, and E. I. F. de Bruijn, 2008: Evaluation of limited-area models for the representation of the diurnal cycle and contrasting nights in CASES-99. *J. Appl. Meteor. Climatol.*, **47 (3)**, 869–887.

Stensrud, D. J., 2007: *Parameterization schemes: keys to understanding numerical weather prediction models*. Cambridge University Press, New York, USA, 480 pp.

Sterk, H. A. M., G.-J. Steeneveld, and A. A. M. Holtslag, 2013: The role of snow-surface coupling, radiation, and turbulent mixing in modeling a stable boundary layer over Arctic sea ice. *J. Geophys. Res.: Atmospheres*, **118 (3)**, 1199–1217.

Stull, R. B., 1988: *An introduction to boundary layer meteorology*. No. 13, Atmospheric and Oceanic Sciences Library, Kluwer Academic Publishers, P.O. Box 17, 3300AA, Dordrecht, The Netherlands.

Stull, R. B., 1993: Review of non-local mixing in turbulent atmospheres: Transilient turbulence theory. *Boundary-Layer Meteorology*, **62 (1-4)**, 21–96.

Sukoriansky, S., B. Galperin, and V. Perov, 2005: Application of a new spectral theory of stably stratified turbulence to the atmospheric boundary layer over sea ice. *Bound.-layer Meteor.*, **117 (2)**, 231–257.

Svensson, G., and J. Lindvall, 2015: Evaluation of near-surface variables and the vertical structure of the boundary layer in cmip5 models. *J. Climate*, **(2015)**.

Tastula, E.-M., B. Galperin, S. Sukoriansky, A. Luhar, and P. Anderson, 2015: The importance of surface layer parameterization in modeling of stable atmospheric boundary layers. *Atmos. Sci. Lett.*, **16 (1)**, 83–88.

Taylor, K. E., 2001: Summarizing multiple aspects of model performance in a single diagram. *J. Geophys. Res.: Atmospheres (1984–2012)*, **106 (D7)**, 7183–7192.

Tewari, M., and Coauthors, 2004: Implementation and verification of the unified NOAH land surface model in the WRF model. *20th conference on weather analysis and forecasting/16th conference on numerical weather prediction*, 11–15, URL https://ams.confex.com/ams/84Annual/techprogram/paper_69061.htm.

Trier, S. B., M. A. LeMone, F. Chen, and K. W. Manning, 2011: Effects of surface heat and moisture exchange on ARW-WRF warm-season precipitation forecasts over the central United States. *Wea. Forecasting*, **26 (1)**, 3–25.

Twine, T. E., and Coauthors, 2000: Correcting eddy-covariance flux underestimates over a grassland. *Agric. For. Meteor.*, **103 (3)**, 279–300.

Van de Wiel, B. J., A. Moene, G. Steeneveld, P. Baas, F. Bosveld, and A. Holtslag, 2010: A conceptual view on inertial oscillations and nocturnal low-level jets. *J. Atmos. Sci.*, **67 (8)**, 2679–2689.

Van der Velde, I. R., G.-J. Steeneveld, B. G. J. Wichers Schreur, and A. A. M. Holtslag, 2010: Modeling and forecasting the onset and duration of severe radiation fog under frost conditions. *Mon. Wea. Rev.*, **138 (11)**, 4237–4253.

Van Heerwaarden, C. C., J. Vilà-Guerau de Arellano, A. F. Moene, and A. A. M. Holtslag, 2009: Interactions between dry-air entrainment, surface evaporation and convective boundary-layer development. *Quart. J. Roy. Meteor. Soc.*, **135 (642)**, 1277–1291.

Warrach-Sagi, K., T. Schwitalla, V. Wulfmeyer, and H.-S. Bauer, 2013: Evaluation of a climate simulation in Europe based on the WRF–NOAH model system: precipitation in Germany. *Climate Dyn.*, **41 (3-4)**, 755–774.

Weller, H., and A. Shahrokhi, 2014: Curl-free pressure gradients over orography in a solution of the fully compressible euler equations with implicit treatment of acoustic and gravity waves. *Mon. Wea. Rev.*, **142 (12)**, 4439–4457.

Whiteman, C. D., and J. C. Doran, 1993: The relationship between overlying synoptic-scale flows and winds within a valley. *J. Appl. Meteor.*, **32 (11)**, 1669–1682.

Wrathall, J. E., 1985: The Mistral and forest fires in Provence-Côte d'Azur, southern France. *Weather*, **40 (4)**, 119–124.

Xie, B., J. C. Fung, A. Chan, and A. Lau, 2012: Evaluation of nonlocal and local planetary boundary layer schemes in the wrf model. *J. of Geophys. Res.: Atmos. (1984–2012)*, **117 (D12)**.

Yang, K., and Coauthors, 2008: Turbulent flux transfer over bare-soil surfaces: characteristics and parameterization. *J. Appl. Meteor. Climatol.*, **47 (1)**, 276–290.

Zängl, G., 2002: An improved method for computing horizontal diffusion in a sigma-coordinate model and its application to simulations over mountainous topography. *Mon. Wea. Rev.*, **130 (5)**, 1423–1432.

Zardi, D., and C. Whiteman, 2013: Diurnal mountain wind systems. *Mountain Weather Research and Forecasting*, Springer Atmospheric Sciences, Springer Netherlands, 35–119.

Zilitinkevich, S., 1995: Non-local turbulent transport: Pollution dispersion aspects of coherent structure of convective flows. *Air Pollution III*, **1**, 53–60.

# LIST OF TABLES

TABLE 1. General settings for all model runs

| | |
|---|---|
| Model version | WRF 3.5.1 |
| Start date | 1200 UTC 18 February |
| End date | 1200 UTC 20 February |
| Time step | 120 seconds |
| Domains configuration | 4 domains (Figure 1) |
| Parent-child ratio | 1 : 3 |
| Nesting | Two-way nested |
| Grid size inner domain | 1 x 1 km |
| Vertical (eta) levels | 35 levels |
| Land use cover | Corine (2006) |
| Global data input | ECMWF analysis 0.25° |
| Microphysics | WSM 6-class (Hong and Lim 2006) |
| Longwave radiation | RRTM (Mlawer et al. 1997) |
| Shortwave radiation | Dudhia (Dudhia 1989) |
| Cumulus scheme | Kain-Fritsch (Kain 2004) |
| Land surface | **Varied** |
| Boundary layer | **Varied** |

TABLE 2. Overview of performed model simulations

| Run # | Surface scheme | Boundary layer |
|---|---|---|
| Run 1 | Noah | YSU |
| Run 2 | Noah | MYJ |
| Run 3 | Noah | QNSE |
| Run 4 | Noah | MYNN2.5 |
| Run 5 | Noah | ACM2 |
| Run 6 | TD | YSU |
| Run 7 | TD | MYJ |
| Run 8 | TD | QNSE |
| Run 9 | TD | MYNN2.5 |
| Run 10 | TD | ACM2 |

TABLE 3. Results of surface layer parameterization experiments. Normalized variance is variance of simulated variable divided by the variance of the observations. Bold numbers indicate best scores.

| | **Default** | **Czil 0.01** | **Czil 1.0** | **sfclay_rev** | **Y08** |
|---|---|---|---|---|---|
| | | **Centered root mean square difference** | | | |
| **T2** ( °C) | 2.48 | **2.36** | 3.09 | 2.68 | 2.64 |
| **T110** (°C) | 2.24 | **2.14** | 2.56 | 2.38 | 2.38 |
| **U10** ($ms^{-1}$) | 0.94 | **0.85** | 1.55 | 0.96 | 1.07 |
| **U110** ($ms^{-1}$) | 2.59 | **2.25** | 2.76 | 2.72 | 2.69 |
| **LW**$^{\downarrow}$($Wm^{-2}$) | **19.87** | 20.01 | 20.07 | 20.37 | 20.44 |
| **LW**$^{\uparrow}$ ($Wm^{-2}$) | 12.14 | 16.48 | 16.82 | **12.09** | 12.13 |
| **H** ($Wm^{-2}$) | 26.90 | 33.87 | **19.51** | 28.09 | 30.33 |
| $L_vE$ ($Wm^{-2}$) | 18.71 | 39.87 | **6.95** | 18.61 | 18.05 |
| **u*** ($ms^{-1}$) | 0.13 | **0.12** | 0.18 | 0.15 | 0.17 |
| | | **Mean overall bias** | | | |
| **T2** (°C) | 1.30 | **1.01** | 1.89 | 1.55 | 1.64 |
| **T110** (°C) | -0.50 | -0.91 | **-0.27** | -0.32 | -0.36 |
| **U10** ($ms^{-1}$) | 1.18 | **1.15** | 1.64 | 1.29 | 1.40 |
| **U110** ($ms^{-1}$) | 1.45 | **1.16** | 1.60 | 1.51 | 1.49 |
| **LW**$^{\downarrow}$ ($Wm^{-2}$) | -19.35 | -20.00 | -18.76 | -18.47 | **-18.29** |
| **LW**$^{\uparrow}$($Wm^{-2}$) | -18.19 | -25.56 | **-1.06** | -18.66 | -17.40 |
| **H** ($Wm^{-2}$) | 7.08 | 9.58 | -12.10 | 6.80 | **3.41** |
| $L_vE$ ($Wm^{-2}$) | 10.99 | 23.99 | **0.83** | 11.74 | 12.68 |
| **u*** ($ms^{-1}$) | 0.12 | **0.09** | 0.18 | 0.11 | 0.13 |

| | | | | | |
|---|---|---|---|---|---|
| | **Correlation coefficient [-]** | | | | |
| **T2** | **0.97** | 0.92 | 0.96 | 0.96 | 0.96 |
| **T110** | **0.96** | 0.95 | 0.94 | 0.95 | 0.95 |
| **U10** | 0.68 | **0.75** | 0.42 | 0.63 | 0.55 |
| **U110** | 0.60 | 0.61 | 0.57 | 0.58 | 0.57 |
| **LW**$^{\downarrow}$ | 0.83 | 0.80 | **0.91** | 0.82 | 0.82 |
| **LW**$^{\uparrow}$ | 0.95 | **0.96** | **0.96** | 0.95 | 0.95 |
| **H** | **0.95** | 0.93 | 0.93 | 0.94 | 0.93 |
| $L_vE$ | **0.92** | 0.91 | **0.92** | **0.92** | **0.92** |
| **u*** | **0.77** | 0.74 | 0.42 | 0.72 | 0.66 |
| | **Normalized variance [-]** | | | | |
| **T2** | **0.56** | 0.67 | 0.44 | 0.53 | 0.53 |
| **T110** | 0.48 | **0.52** | 0.41 | 0.45 | 0.45 |
| **LW**$^{\downarrow}$ | 0.29 | **0.30** | 0.24 | 0.27 | 0.26 |
| **LW**$^{\uparrow}$ | **0.81** | 0.60 | 1.32 | **0.81** | **0.81** |

# LIST OF FIGURES

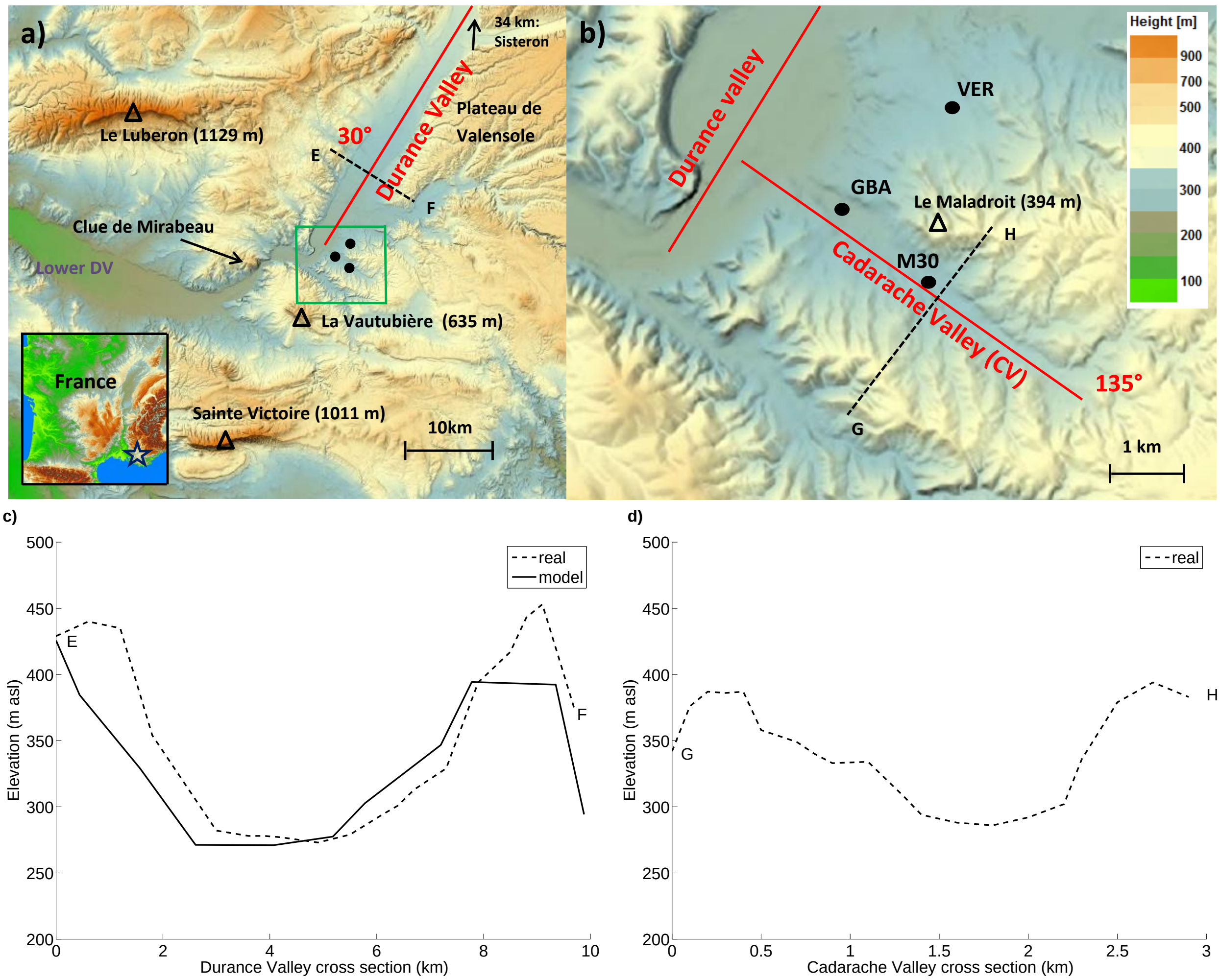


FIG. 1. A: The Durance valley area with important orographic features and its location in southeastern France. B: Zoom of the Caradache area (green rectangle in A), with measurement locations. VER is La Verrerie (295 m asl), the location of the SODAR and meteostation, GBA is the Grande Bastide (265 m asl) where the 110 m mast is installed and M30 is the location of the 30 flux-tower (286 m asl) and the launch site for radiosoundings and tethered balloon. C: Cross-section of the Durance valley elevation at the location of the dashed line in (A). The WRF elevation is plotted in this figure as well. D: Cross-section of the Cadarache valley elevation at the location of the dashed line in (B). This valley is not resolved in WRF at 1 km grid spacing.

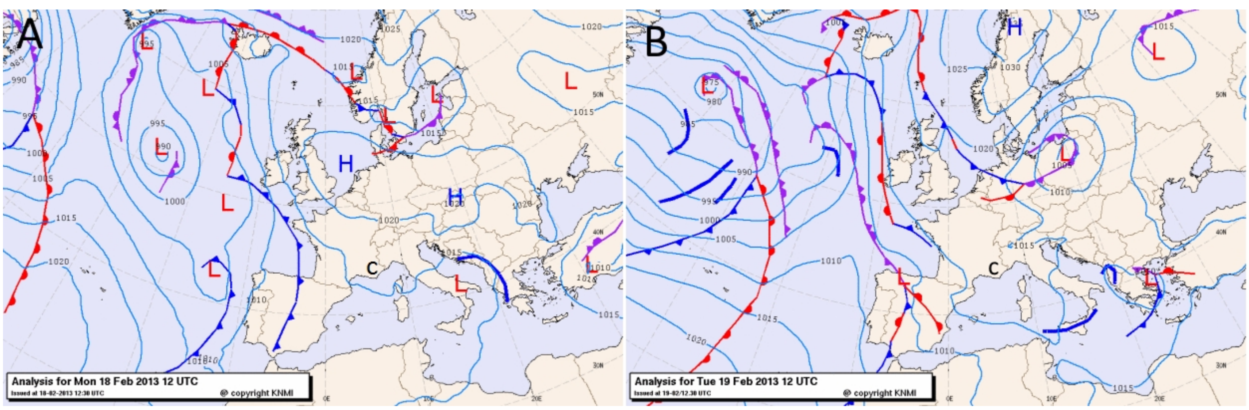


FIG. 2. Operational analysis at (A) 18 February 1200 UTC and (B) 19 February 1200 UTC. Cadarache is indicated with a 'C'. Source: KNMI.

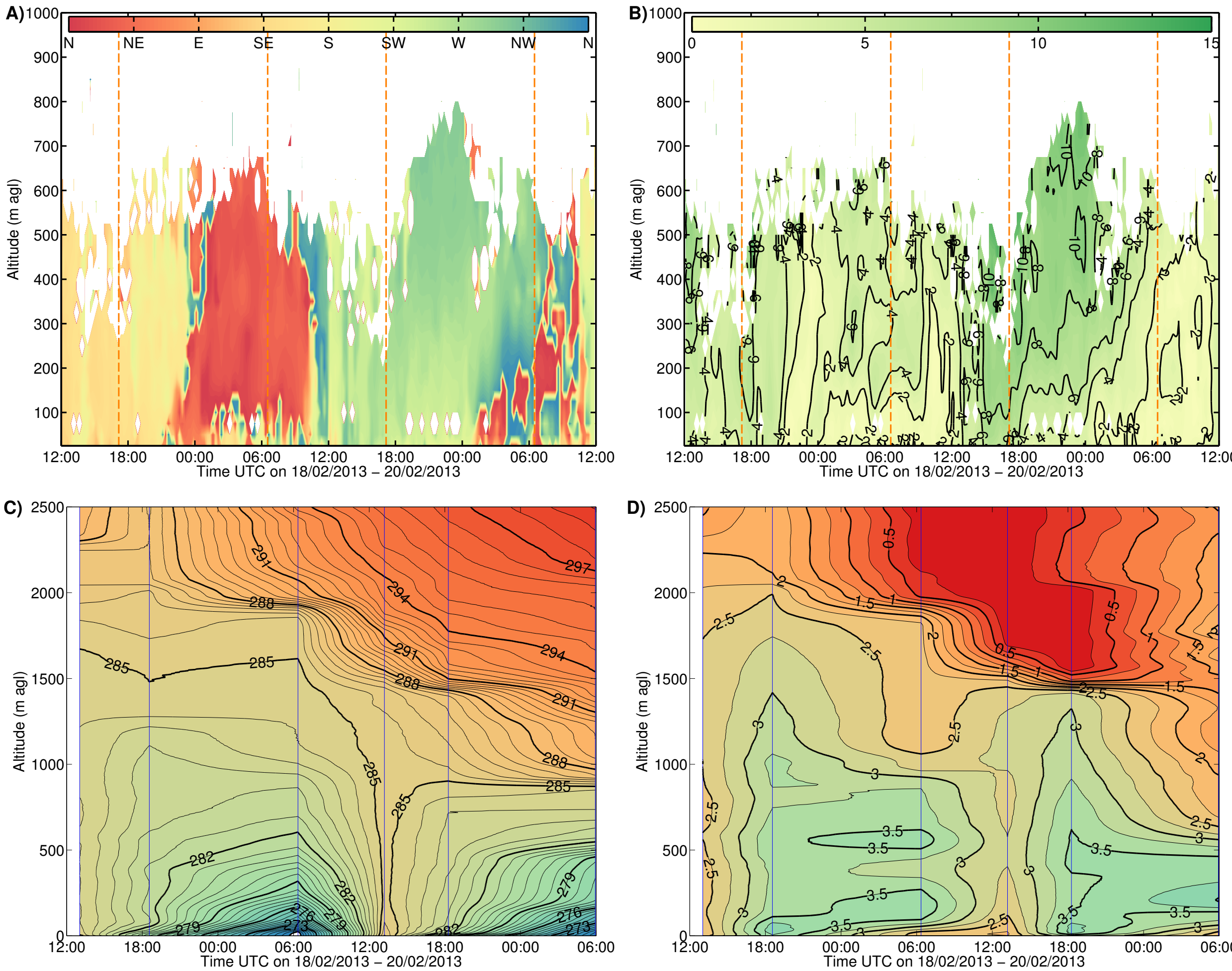


FIG. 3. Observed evolution of A) wind direction and B) wind speed, measured by the SODAR, and C) potential temperature (K) and D) mixing ratio (g kg$^{-1}$) during IOP15 and IOP16. The vertical lines in the lower two plots indicate radiosoundings between which the variables are interpolated. Note that sounding data after 0600 UTC 20 February is lacking. In A) and B), the orange vertical lines represent the times of sunset and sunrise. Note that the color scale is not cyclic, so the strong gradient around the north component is somewhat misleading.

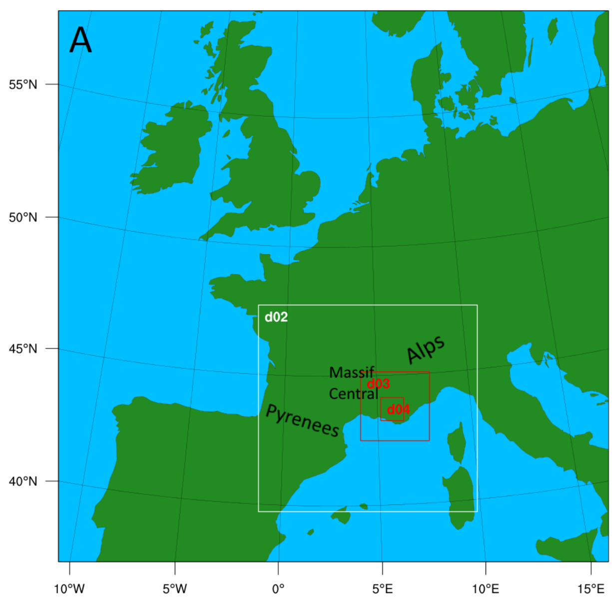


FIG. 4. WRF domain configuration. The bounds of the outer domain coincide with the border of the figure. The most important orographic features are indicated with text. Grid spacing from outer (D01) to inner (D04) domain is 27, 9, 3 and 1 km.

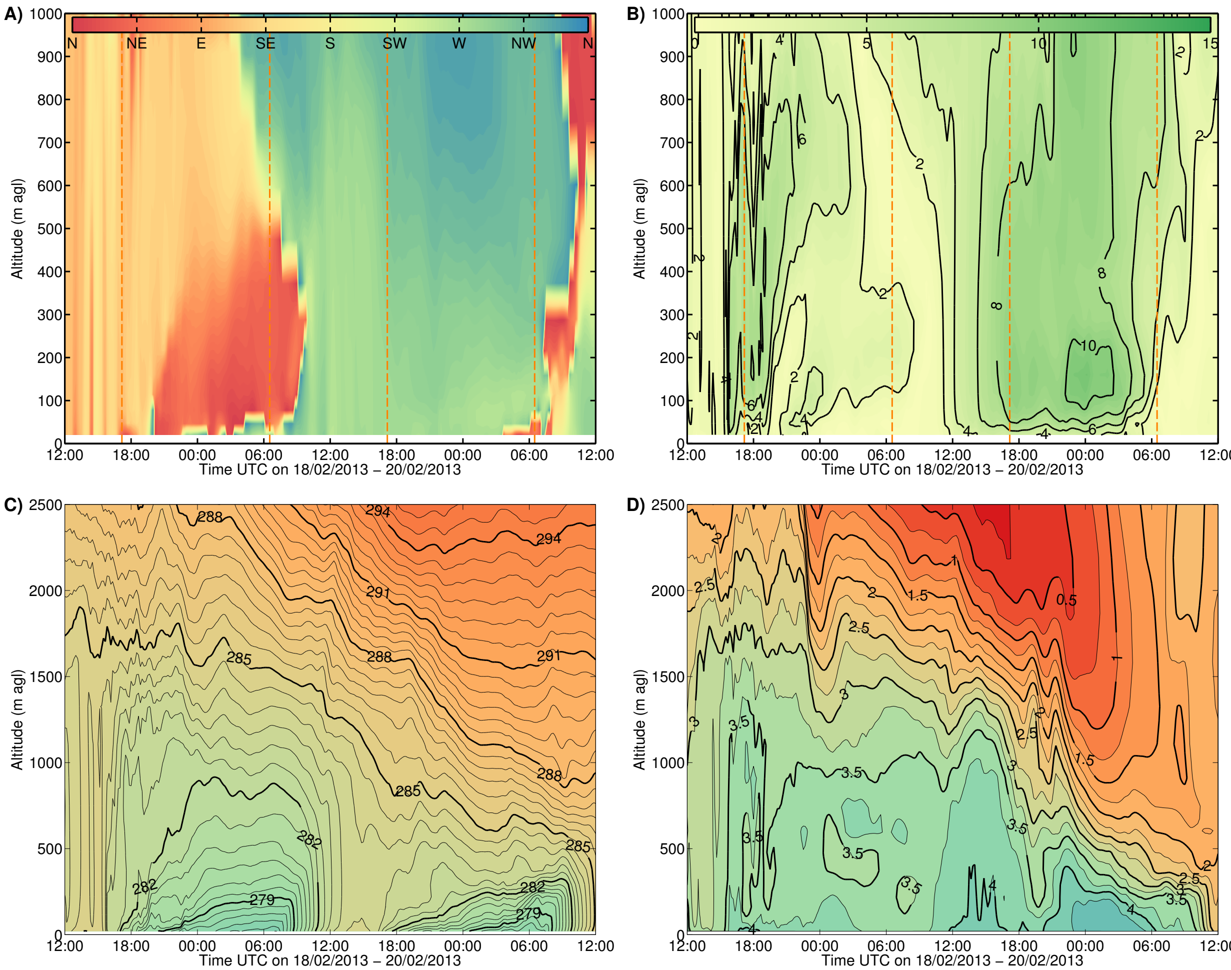


FIG. 5. Same as Figure 3, for model output from run with revised surface layer scheme and RRTMG radiation. Note that in C) and D), the time axes are extended until 1200 UTC.

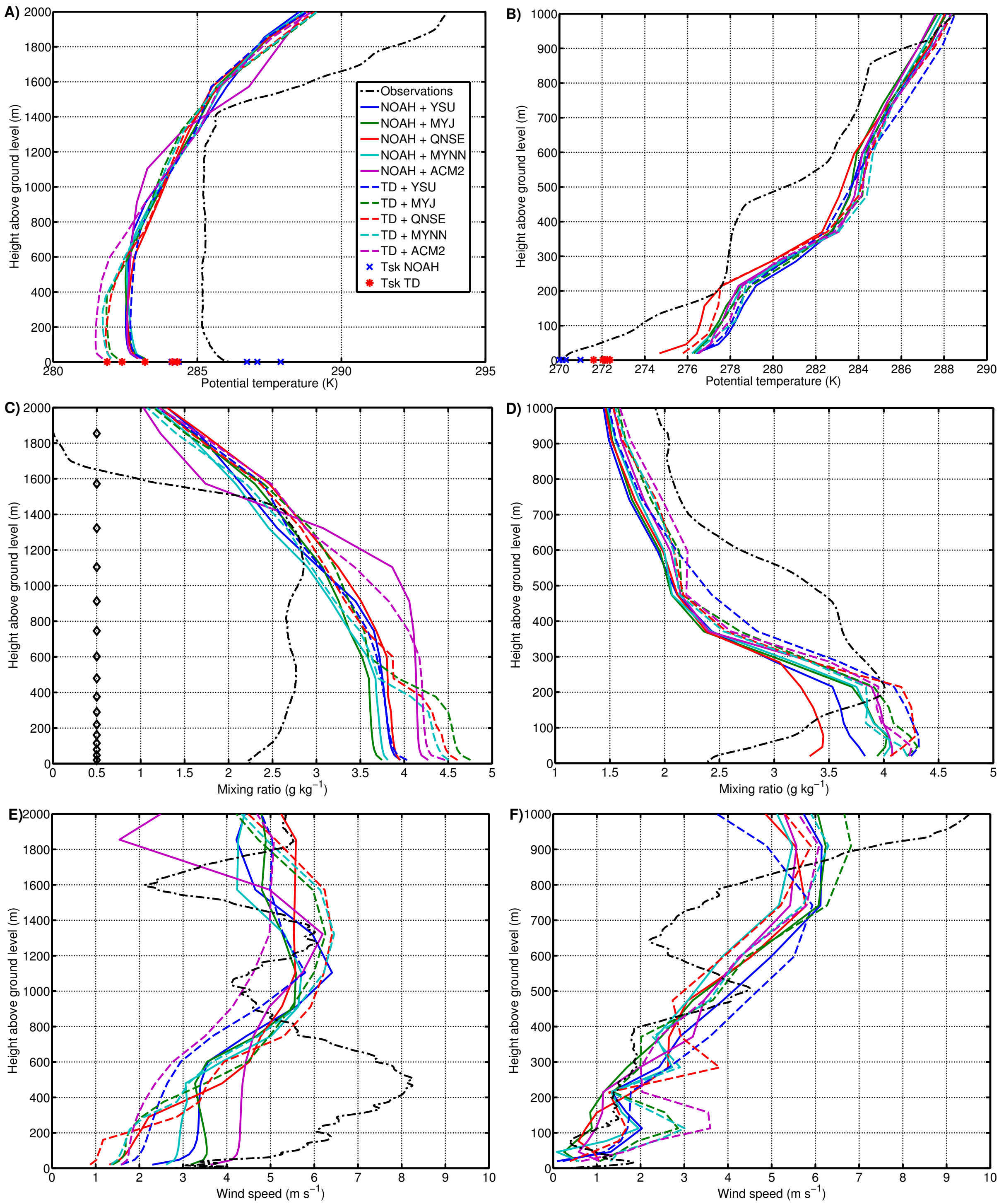


FIG. 6. Observed and modelled profiles of A) potential temperature at 1200 UTC 19 February and B) at 0600 UTC 20 February, mixing ratio (C and D) and wind speed (E and F) at the same times. Simulated $T_s$ is indicated in A) and B). Diamonds in C) indicate WRF vertical levels. Note that the axes are different at 1200 and 0600 UTC.

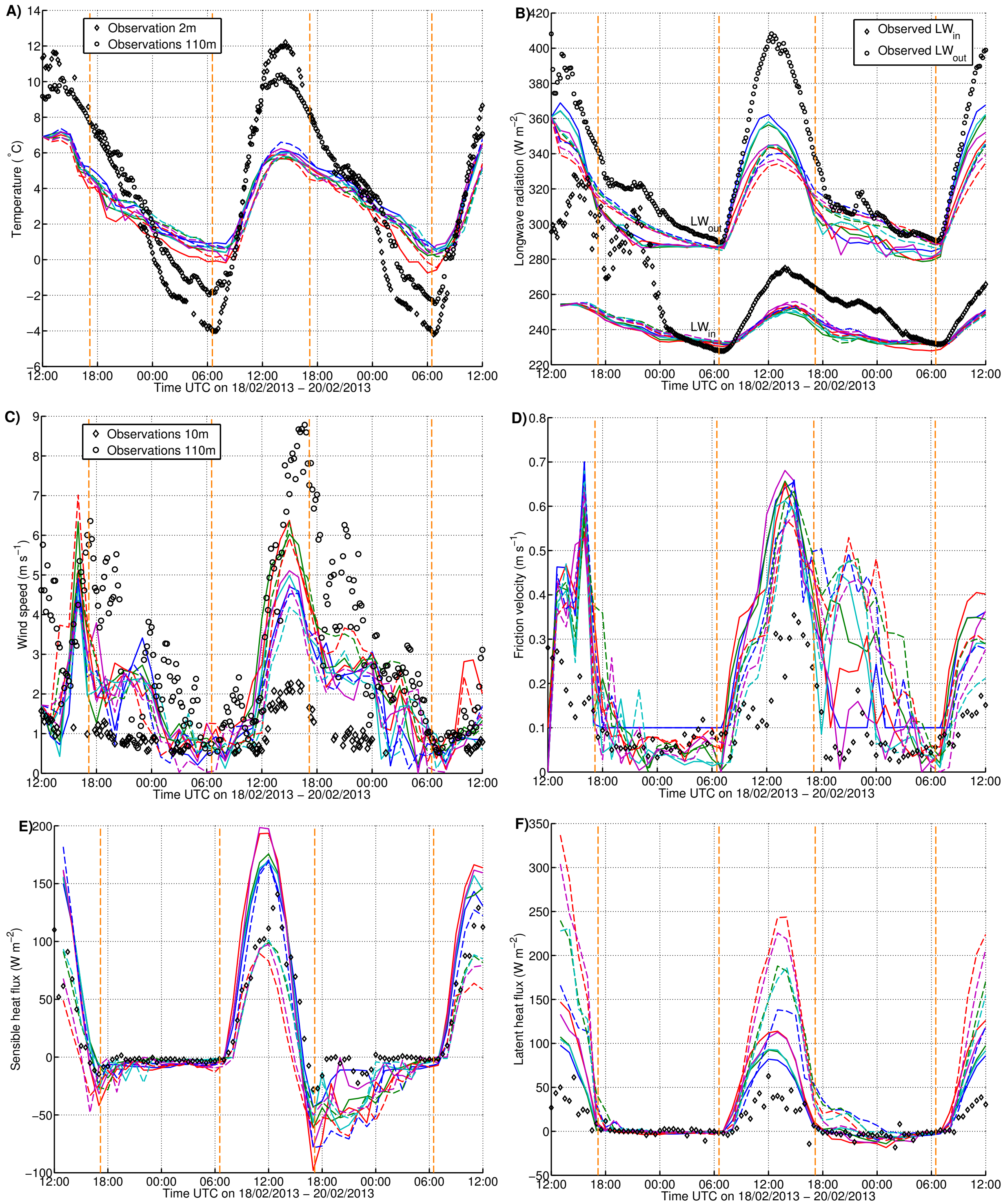


FIG. 7. Modelled and measured evolution of A) 110 m temperature, B) longwave radiation components, C) 10 m wind, D) friction velocity, E) sensible heat flux and F) latent heat flux. Legend same as in Figure 6. All observations are from M30 site, except for wind which is from GBA (110 m) and VER (10 m).

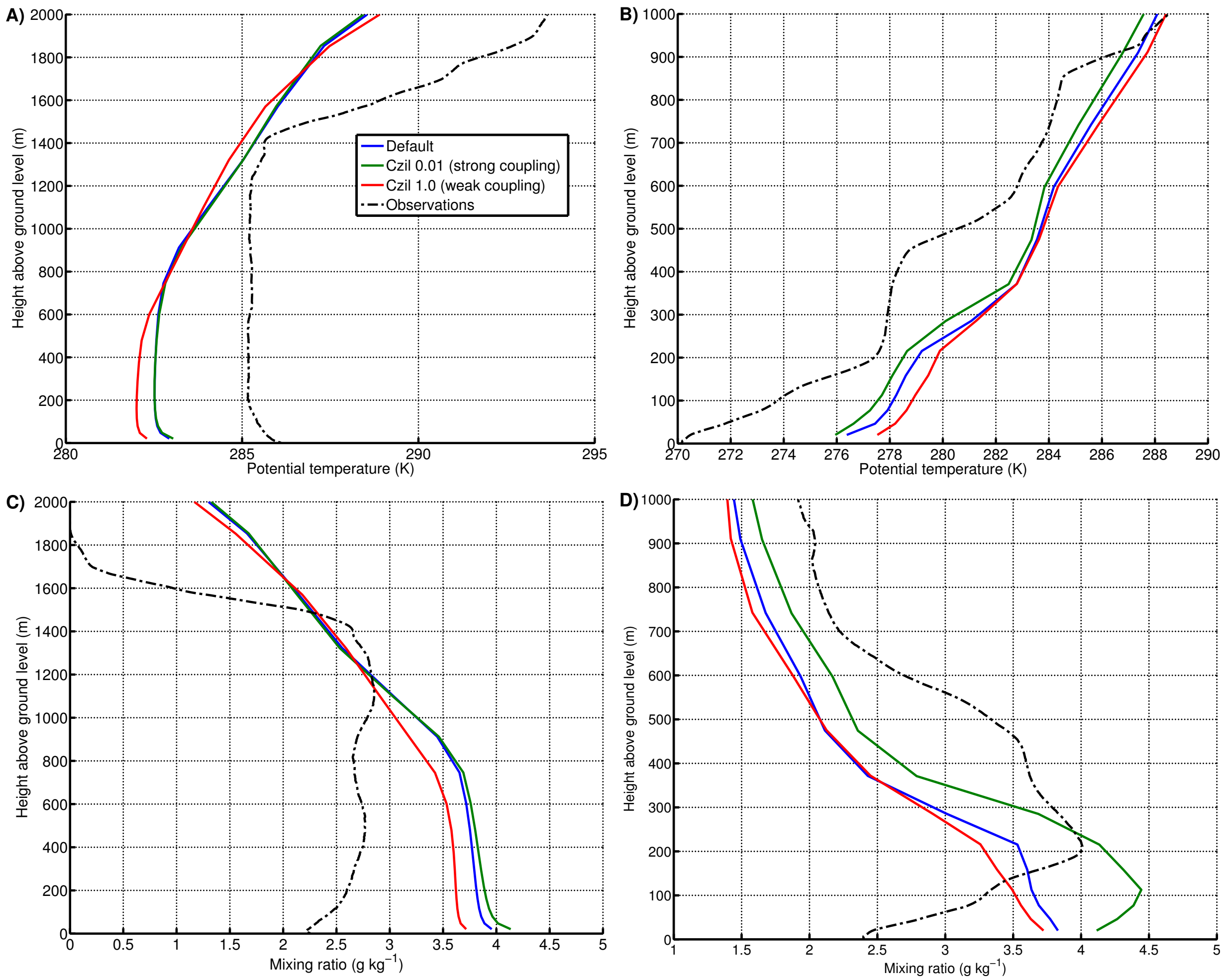


FIG. 8. Same as Figures 6A-D for reference, strong and weak surface coupling

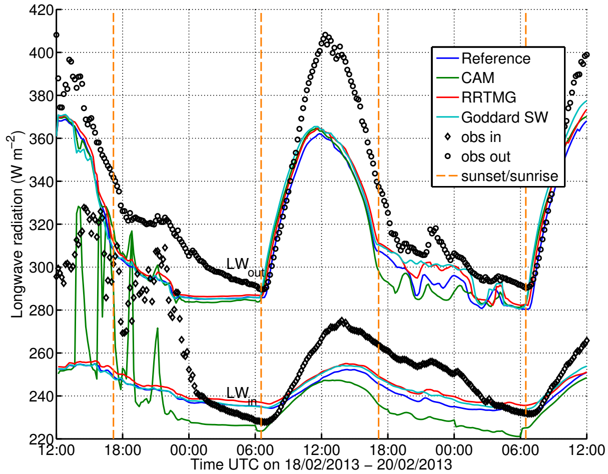


FIG. 9. Modelled (three radiation schemes) and observed longwave radiation components. Reference is Noah+YSU with revised surface layer scheme (sfclay_rev).

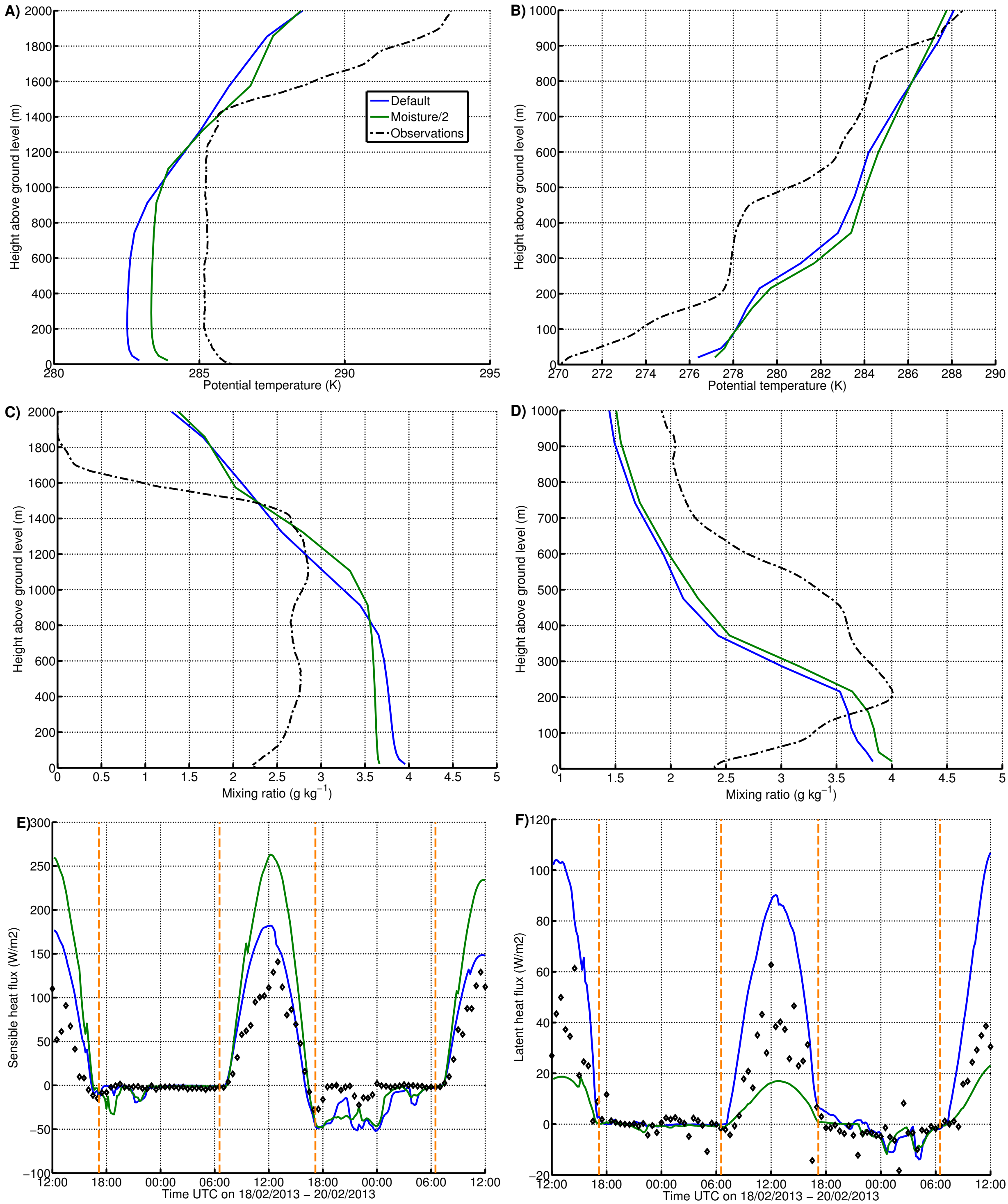


897 FIG. 10. A-D same as Figures 6A-D; E and F same as Figures 7E and F, for reduced soil moisture. Reference

898 refers to the original reference run but with revised surface layer scheme (sfclay_rev) and RRTMG radiation.